



**HAL**  
open science

## Synthesis and characterization of a $\text{Sb}_2\text{Te}_3/\text{Bi}_2\text{Te}_3$ p-n junction heterostructure via electrodeposition in nanoporous membranes

Rashmi Rani, Sandrine Tusseau-Nenez, Pierre-Eugene Coulon, Travis L. Wade, Marcin Konczykowski

### ► To cite this version:

Rashmi Rani, Sandrine Tusseau-Nenez, Pierre-Eugene Coulon, Travis L. Wade, Marcin Konczykowski. Synthesis and characterization of a  $\text{Sb}_2\text{Te}_3/\text{Bi}_2\text{Te}_3$  p-n junction heterostructure via electrodeposition in nanoporous membranes. *iScience*, 2021, 24 (6), pp.102694. 10.1016/j.isci.2021.102694. hal-03799191

**HAL Id: hal-03799191**

**<https://hal.science/hal-03799191>**

Submitted on 2 Aug 2023

**HAL** is a multi-disciplinary open access archive for the deposit and dissemination of scientific research documents, whether they are published or not. The documents may come from teaching and research institutions in France or abroad, or from public or private research centers.

L'archive ouverte pluridisciplinaire **HAL**, est destinée au dépôt et à la diffusion de documents scientifiques de niveau recherche, publiés ou non, émanant des établissements d'enseignement et de recherche français ou étrangers, des laboratoires publics ou privés.



Distributed under a Creative Commons Attribution - NonCommercial 4.0 International License

# Synthesis and characterization of a $\text{Sb}_2\text{Te}_3/\text{Bi}_2\text{Te}_3$ p-n junction hetero-structure via electrodeposition in nanoporous membranes

Rashmi Rani<sup>1,3\*</sup>, Sandrine Tusseau-Nenez<sup>2</sup>, Pierre-Eugene Coulon<sup>1</sup>,

Travis. L. Wade<sup>1</sup>, Marcin Konczykowski<sup>1</sup>

<sup>1</sup>Laboratoire des Solides Irradiés, UMR 7642 CEA-CNRS-Ecole polytechnique.

<sup>2</sup>Laboratoire de Physique de la Matière Condensée, UMR 7643 CNRS-Ecole polytechnique.

<sup>3</sup> Lead contact

\*Corresponding author: [newton\\_rashmi51@yahoo.com](mailto:newton_rashmi51@yahoo.com) (Rashmi Rani)

## SUMMARY

Topological insulators (TIs) are bulk insulators with a metallic surface states that can be described by a single Dirac cone. However, low-dimensional solids such as nanowires (NWs) are a challenge, due to the difficulty of separating surface contributions from bulk carriers. Fabrication of nanowires with high surface to volume ratio can be realized by different methods such as chemical vapor transport, molecular beam epitaxy and electrodeposition. The last method is used in the present work allowing the growth of structures such as p-n junctions, intercalation of magnetic or superconducting dots.<sup>[step]</sup> We report the synthesis of high-quality TI nanowire:  $\text{Bi}_2\text{Te}_3$ ,  $\text{Sb}_2\text{Te}_3$  and p-n junction via electrodeposition. Structural, morphological and nano structure properties of nanowires have been investigated by various characterization techniques. Interface structures and lateral hetero junctions (LHJ) in p-n junction NWs has also been made.

**Keywords:** Electrodeposition, topological insulator nanowires (TIs NWs), STEM, interface structures, lateral hetero junctions (LHJ), spin-coating.

## INTRODUCTION

Discovery of new class of materials named TIs initiated intense research motivated by the novel physical properties of TI's and perspectives for device applications in spintronics and quantum computation processing [Hasan and Kane, 2010; Hasan and Moore, 2011; Luo et al., 2013; Le et al., 2014; Tu et al., 2015]. Electronic band structure of those materials is fully gapped in the bulk, but with unusual gapless 'protected' 2D Dirac surface state [Liu et al., 2019; Moore, 2010; Qi and Zhang, 2011]. This band structure arises in compounds containing high atomic mass elements with strong spin-orbit (SO) coupling. This prediction was followed by several experiments, Angular Resolved Photo Emission Spectroscopy (ARPES) and Scanning Tunneling Microscopy (STM) demonstrating locked spins [Alpichshev et al., 2010; Chen et al., 2009; Hsieh et al., 2009; Wang et al., 2011; Zhang et al., 2009].

The presence of topologically protected and spin-locked surface states inhibits backscattering and leads to very long dephasing lengths. These systems could be promising in the field of spintronics and fault-tolerant quantum computing. However, access to this 2D quantum matter is a challenge, due to the difficulty of separating surface contributions from the non-conductivity of the bulk. In approaches taken thus far, such as nano-structured synthesis/growth, doping, compositional tuning, or band- gap engineering via device gating, complete suppression of the bulk conduction in TIs has not yet been realized. Existence of Dirac cone type surface states was found in several systems, and one can distinguish several classes of TI's. Time reversal symmetry protected family represented by layered  $\text{Bi}_2\text{Te}_3$ ,  $\text{Bi}_2\text{Se}_3$ ,  $\text{Sb}_2\text{Te}_3$ , and crystal symmetry protected, cubic  $\text{Pb}_{1-x}\text{Sn}_x\text{Se}$ ,  $\text{SnTe}$ , and Kondo type  $\text{SmB}_6$ .

Electronic transport properties specific to the surface conduction channel are difficult to separate from bulk conductivity. In most cases, linear in field magneto resistance due to weak anti-localization and Berry phase in Shubnikov-de Hass oscillations are observed on the large background. This jeopardizes verification of theoretical predictions of novel quantum effects such as Majorana fermions on the interface between TI and superconductor, Klein tunneling and Mach-Zehnder interferometer on TI based p-n junction. The main obstacle is the fabrication of high-quality TI materials and structures.

Nano scale topological insulator has a large surface-to-volume ratio that can manifest the conductive surface states and are promising candidates for devices [Guo et al., 2015; Hong et al., 2014; Ilan et al., 2015; Kong et al., 2010.]. There are number of studies focused on the fabrication and characterization of thin-films and nanoplates [Fei et al., 2015; Jiang et al., 2015; Le et al., 2017; Zhang et al., 2012.], much less attention has been given to the TIs nanostructured such as nano wires (NWs), nanorods, nanotubes [Eschbach et al., 2015; Krieg et al., 2019; Zuev et al., 2010.]. Three different technological methods are commonly used to produce TI NWs: photolithography, vapor transport with seed and template electro-deposition growth. The last approach offers a less expensive and convenient way to fabricate periodically aligned NWs with uniform diameter which is very useful for nanostructured electronic applications [Pinisetty et al., 2011]. It also has considerable advantages over other methods in fabrication of complex hetero-structures such as p-n junctions, interfaces with magnetic or superconducting materials. Although no systematic study of the layered structure ( $\text{Sb}_2\text{Te}_3/\text{Bi}_2\text{Te}_3$ ) in p-n junction TIs NWs has been performed.

In this article, we present a convenient method to fabricate the p-n junction TIs NWs with defect free interface by electrodeposition. We also discuss on comparative studies of structural and

morphological properties of  $\text{Bi}_2\text{Te}_3$ ,  $\text{Sb}_2\text{Te}_3$  and p-n junction TIs NWs. We believe that our results add a new approach for further study of interface structure in p-n junction NW. To the best of our knowledge this is the first report on the lateral heterojunction in  $\text{Sb}_2\text{Te}_3/\text{Bi}_2\text{Te}_3$  p-n junction TIs NW.

## RESULTS AND DISCUSSIONS

### Nano structural analysis of $\text{Bi}_2\text{Te}_3$ , $\text{Sb}_2\text{Te}_3$ and p-n junction NWs

X-ray diffraction (XRD) patterns of  $\text{Bi}_2\text{Te}_3$ ,  $\text{Sb}_2\text{Te}_3$  and p-n junction TIs NWs embedded in polycarbonate template [Figure S1(A), (B) and (C)] show diffraction peaks of all the three samples correspond to the rhombohedral phase with R3 space group of  $\text{Bi}_2\text{Te}_3$  (JCPDS card: 00-015-0863),  $\text{Sb}_2\text{Te}_3$  (JCPDS: 00-015-0874) and p-n junction. The peaks from gold (JCPDS card 00-04-0784) are clearly observed. The peak around  $2\theta \sim 17.2^\circ$  (shown by \*) corresponds to two peaks, one from the sample and other from the polycarbonate membrane so we decided to focus our analysis only on pure peaks of the samples. XRD patterns of  $\text{Bi}_2\text{Te}_3$  [Figure S1(A)] and  $\text{Sb}_2\text{Te}_3$  [Figure S1(B)] are mostly similar and there is no trace of any secondary phase was found although broadening in the background has been detected for  $\text{Sb}_2\text{Te}_3$  nanowires which could be attributed to amorphous phase or poor crystallinity exist in the antimony telluride. The peak (015) for both samples  $\text{Bi}_2\text{Te}_3$  and  $\text{Sb}_2\text{Te}_3$ , indicating a highly preferential orientation of the NWs along the [015] direction and the same orientation maintained in the p-n junction NWs [Figure S1(C)]. Figure 1A shows the comparison of XRD of three samples. In Figure 1B clearly the strong peaks (015) of both  $\text{Sb}_2\text{Te}_3$  and  $\text{Bi}_2\text{Te}_3$  are well observed in the p-n junction,

indicating the nice phase separation in the sample. However, a small shift of peaks has been found  $\sim 0.03^\circ$  which is small enough to consider error bar in XRD analysis. Figure 1C depicts that all observed peaks of  $\text{Bi}_2\text{Te}_3$  and  $\text{Sb}_2\text{Te}_3$  are present in p-n junction which indicating bi-metal structure. In addition, we noticed that the peaks oriented in (110) are broader than the peak (015) indicating a smaller crystallite size or a greater lattice strain more effective in [110] direction. To investigate the lattice strain and crystallite size of the wires, we followed the procedure recommended by Langford [Langford & Wilson, 1978]. Here we used the Halder-Wagner plots for analyzing the crystallite size ( $D_v$ ) and microstrain ( $\epsilon$ ) of the wires (discuss in next section microstructure analysis). Figure 1D clearly shows, for each of the three samples, that the points are aligned along a line without y-intercept (or very small value), indicating that the broadening is mainly due to a crystallite size effect. In that case, the Scherrer formula can also be used to extract the average crystallite size, according to the well-known formula:

$$\beta = K \lambda / (D \cos\theta)$$

Where  $K = 1.0747$  is the Scherrer's constant (in the case of the use of integral breadth ( $\beta$ ) to characterize the broadening). It can be seen that the calculated value of crystallite size agreed well with the two approaches [Table 1] and an anisotropy in size is observed on Halder-Wagner plots. Considering the weak intensities of the peaks, the calculated crystallite sizes should be taken as tendency instead of absolute values, while the average value  $\sim 30$  nm is well corresponded with the diameter of the polycarbonate membrane.

Moving now to explaining the morphology and crystallinity of the  $\text{Bi}_2\text{Te}_3$ ,  $\text{Sb}_3\text{Te}_3$  and p-n junction NWs. Figure 2(A-F) which clearly display the uniformity in morphology with the smooth surface for all the three samples which makes them good candidate for future fabrication of a nanostructured devices. High resolution TEM and SAED patterns with shiny fringes [Figure

S2 (A) and Figure S3] for  $\text{Bi}_2\text{Te}_3$  shows a good crystallinity and can be indexed to the rhombohedral crystal structure (JCPDS card no. (15-0863) with the lattice spacing of the shell is 1.49 Å corresponding to the [1115] plane which is in good agreement with XRD. On the contrary for the antimony telluride we found that most of the nanowires are completely amorphous [Figure S4(D)]. While few of them are the mixture of amorphous and crystalline phase [Figure S4(E)]. Notably crystalline phase corresponds to the rhombohedral crystal structure (JCPDS card no. (15-0874) with the lattice spacing of the shell is 3.29 Å corresponding to the [015] plane which matches with the most intense peak of XRD [Figure S1(B)]. Through careful investigation, as discuss in later section (Structural and chemical analysis of antimony telluride), amorphous phase was also found in XRD although crystalline phase was well observed with pure intense peaks which arouses the fact that crystalline phase could be improved and possibly antimony telluride could be maintain the layered structure in p-n junction and provide us with the opportunity to further investigate their electronic properties through this structure.

### **Microstructure analysis**

The recommended procedure:

Computing the integral breath (IB) and the full width at half maximum (FWHM) of a pseudo-Voigt curve from the broadened profile to obtain the shape factor ( $Q = \text{FWHM}/\text{IB}$ ), calculating the breadths of the constituent profiles corrected for instrumental broadening (using NIST LaB6 standard to determine the instrumental broadening using the Caglioti function) and analyzing the Williamson-Hall and Halder-Wagner plots [Izumi and Ikeda, 2004]. These plots are a very useful overview of the microstructural properties of the sample, highlighting possible anisotropic



behaviour according to (hkl) planes and giving an approximate values of the crystallite size  $D_v$  (volume-weighted average size) and microstrain  $\epsilon$  (r.m.s) for root mean square of the variation in the lattice parameter due to the effect of several defects.

The well-known Williamson-Hall plot follows the equation:

$$\beta \cos\theta / \lambda = C\epsilon \sin\theta / \lambda + K/D \quad (1)$$

A slope close to zero indicates that the broadening is due to crystallite size effect only, with crystallites exhibiting an average spherical shape.  $C = 2$  and  $K = 4/3$  are recommended by Izumi et al., assuming the hypothesis of a spherical crystallite shape [Izumi et al., 2003].

When this approach is used with Lorentzian peak shape), a negative microstrain can be obtained that is not physically meaningful. For the determination of  $D_v$  and  $\epsilon$ , Halder and Wagner [Halder and Wagner, 1966] proposed an alternative equation adapted for  $0.663662 < \phi < 0.93949$  corresponding to the pseudo-voigt function containing the integral breadth,  $\beta^*$  of the reciprocal lattice point ( $\beta^* = \beta \cos\theta / \lambda$ ) and the lattice plane spacing,  $d^*$  for the reciprocal cell ( $d^* = 2 \sin\theta / \lambda$ ) as:

$$(\beta^* / d^*)^2 = K/D \cdot \beta^* / (d^*)^2 + (2\epsilon)^2 \quad (2)$$

The value of  $K = 4/3$  is believed to be valid for the size (as the volume-weighted average) of spherical crystallites [Langford and Wilson, 1978]. This equation does not contain the constant  $C$ , for which the value is still under discussion. As our factors were calculated between ( $\phi < 0.63662$ ) we selected HW method for our study.

### **Structural and chemical analysis of antimony telluride**

In this study we have analysed the structure and the chemical composition of antimony telluride ( $\text{Sb}_2\text{Te}_3$ ) nanowires by using X-Ray Diffraction (XRD) and Transmission Electron Microscopy (TEM).

Figure S1(B) shows the XRD of  $\text{Sb}_2\text{Te}_3$  nanowires imbedded in polycarbonate membrane. We can see the well-defined peaks, corresponding to the crystalline phase (JCPDS 15-0874) excepted the broadening in background. This may be due to the polycarbonate membrane Figure S4(B) but by careful investigation we detected the broadening in the base of the main peak (015) which is due to the sample [Figure S4(A), inset Figure S4(B)], it can be explained by the existence of amorphous phase in the antimony telluride. Furthermore, the composition difference between index  $\text{Sb}_2\text{Te}_3$  and sample observed is confirmed by EDX [Figure S4(C)] which indicates a stoichiometry of the sample nearly  $\text{Sb}_3\text{Te}$ .

With (SAED) and (HRTEM) we can see that the majority of antimony telluride nanowires are amorphous [Figure S4(D) & Figure S4(E)]. Nevertheless, a few nanowires are crystalline in the core, as can be seen in [Figure S4(E)]. This crystalline phase corresponds to  $\text{Sb}_2\text{Te}_3$  phase (JCPDS 17-0874). Some reports said that at room temperature it is common to find noncrystalline / amorphous structure for  $\text{Sb}_2\text{Te}_3$  which can be transformed to the crystalline structure by the annealing [Kim and Oh, 2010]. It has also been reported that it is difficult to synthesize compositionally controlled crystalline  $\text{Sb}_2\text{Te}_3$  by electro-deposition [Lensch-Falk et al., 2012].

Overall XRD and TEM experiments bring out the presence of both amorphous and crystalline phases in antimony telluride nanowires however crystalline phase was dominated in XRD. It has been also observed stoichiometric defects or impure phase in the antimony telluride which is quite common for electrodeposition due to deposition potential and it could be improve during

the deposition. Since the electrodeposition was carried out at the room temperature which could be the reason for amorphous phases in antimony telluride nanowires.

### **Layer structured p-n junction NWs analysis**

Grazing incidence- XRD (GIXRD) technique was used to study the layer of  $\text{Sb}_2\text{Te}_3$  and  $\text{Bi}_2\text{Te}_3$  in p-n junction NW represented systematically in Figure 3A [see in Supplemental Material, Figure S5(A) & (B)]. The p-n junction sample was made in order to obtain a layered structure as depicted in Figure 3B and C. In this experiment we use grazing angle ( $\omega$ ) starting from  $3^\circ$  to  $6^\circ$  to see the layer structure in the p-n junction, Figure 3D. At  $\omega=4^\circ$  we clearly observed the peaks only for  $\text{Sb}_2\text{Te}_3$ : (PDF 15-0874), indicating the first layer of the p-n junction [Figure S6 (A)]. The peaks for  $\text{Bi}_2\text{Te}_3$  (PDF 15-0683) have been found when ( $\omega$ ) is increasing up to  $5^\circ$  [Figure S6 (B)]. Once ( $\omega$ ) reached  $7^\circ$ , GIXRD shows peaks for gold (PDF 65-2870) that defines surface of the substrate [Figure S6 (C)]. Interestingly, we can see that the crystal structure of  $\text{Sb}_2\text{Te}_3$  and  $\text{Bi}_2\text{Te}_3$  in p-n junction remain the same as the pure phase, indicating that formation of p-n junction does not lead to the formation of a ternary phase made by  $\text{Sb}_2\text{Te}_3$  and  $\text{Bi}_2\text{Te}_3$ . No evidence of solid solution was detected in the p-n junction which may explain the abrupt interface between p and n-type.

To investigate the interface structure in p-n junction NWs, we performed STEM. Figure 4A Depicts an elemental mapping by EDX of the p-n junction. STEM measurement reveals that the NW has two compounds:  $\text{Sb}_2\text{Te}_2$  and  $\text{Bi}_2\text{Te}_3$  which respectively correspond to p and n types layered structure in p-n junction NW. Figure 4B shows the homogeneous spatial distribution of the Bi and Sb elements in the p-n junction NW as well as the presence of Te throughout the

whole wire. The two-contrast dark and bright were respectively found to be composed of  $\text{Sb}_2\text{Te}_3$  and  $\text{Bi}_2\text{Te}_3$  in Figure 4C due to the difference of the mean atomic numbers of both regions. This contrast change is also observed in boundary of the NW which implies the loss of resolution at the edge of the wire [Fang et al., 2013]. Notably, existence of lateral heterojunction (LHJ) ( $\text{Sb}_2\text{Te}_3/\text{Bi}_2\text{Te}_3$ ) in transition region has been observed (shown by dotted line) which was also reported by [fei et.al, 2015]. In topological insulator physics LHJs play a more interesting role than vertical ones because new interface state generated between two SS region in the same plane [Hasan and Kane, 2010; Ilan et al., 2015]. Additionally, we can see the explicit interface of the lateral layers ( $\text{Sb}_2\text{Te}_3/\text{Bi}_2\text{Te}_3$ ) in p-n junction which proves that our strategy to control over the mixture between two layers in transition region during the synthesis by depositing the amount of initial precursor is quite successful.

The STEM of the p-n junction gives additional information on the interface. First, STEM-HAADF imaging brings out the fact that the transition between bismuth telluride and antimony telluride is sharp from a chemical point of view, clearly evidenced by the difference in contrast between the n and the p types regions. Second, we can see that this slantwise interface is not flat and presents some rugosity from one side of the nanowire to the other. This is clearly evidenced by the STEM-HAADF imaging and can explain the origin of the apparent Bi and Sb intermixing on the STEM-EDX mapping Figure 4D.

### **p-n junction NWs synthesis for electronic application**

According to requirement of the electronic applications, we used AAO porous membrane for getting long and perfectly cylindrical NWs and we performed SEM to investigate influences of AAO membrane on the growth of the NWs. [Figure S7] depict that the p-n junction NWs with large quantity obtained after dissolving the membrane illustrate the nanowires with smooth

contours and have a narrow size distribution with a diameter around 80 nm as expected. The length of the nanowires ranges tens of microns to few millimeters, suggesting that the 100% growth of nanowires. Figure 5A shows the top view of the p-n junction nanowires after dissolving the template in aqueous NaOH solution. Only a few pores remain blank. The filling ratio is quite higher than the porosity of the template. To get single dispersed p-n junction NW for further application followed by lithography, we used spin-coating technique (depicted as Figure 5B). Concentrated p-n NW suspension in ethanol was diluted by about one thousand times. The suspension was deposited on to the silicon wafer by spin coating at the rotatory speed of 1000 rpm. It can be noted that uniform distribution of nanowires has been obtained Figure 5C may be due to the balance between centrifugal force and viscous force of the liquid in the spin coating process [Xie et al., 2013]. When we increased the rotatory speed to 2000 rpm Figure 5D interestingly a unique morphology of the p-n junction nanowires is discovered which are referred to as zig-zag nanowires. It may be due to the viscous force which is lower than centrifugal force due to the high rotatory speed. It has also been reported that the appearance of zig-zag morphologies comes from the partially low surface-interfacial energy on the surface of the droplets [Park and Lee, 2014]. Some other reports show that low surface interfacial energy break the continuous straight growth of nanowires [Ma et al., 2004; Moore and Balents, 2007]. This cause some p-n NWs break into small pieces but still some of them have length of 5-7  $\mu\text{m}$  which could be used for applications. Since NWs are completely detached with one another they shall be used for four probe measurements followed by photo lithography which is the object of a forthcoming publication.

## CONCLUSIONS

In conclusion, we explored the comparative analysis of structural and morphological properties of  $\text{Bi}_2\text{Te}_3$ ,  $\text{Sb}_2\text{Te}_3$  and p-n junction NWs. We have demonstrated for the first time a template-based growth strategy for the synthesis of hetero-structure ( $\text{Sb}_2\text{Te}_3/\text{Bi}_2\text{Te}_3$ ) p-n junction NWs, employing electrodeposition as the synthesis method. We have also described the layer structure in p-n junction NWs by GIXRD technique. STEM reveals several important points; first, p-n junction has two compositions p and n type; second, existence of lateral hetero junction in the transition region has been identified; third, sharp interface about  $\leq 10$  nm has been explored which was observed first time in electrodeposition template growth. Thus, we believe that the growth of the p-n NWs with explicit interface would have profound potential for offering a promising building block for next generation spintronics devices. Spin-coating technique has been applied for dispersing p-n junction NWs and finding individual one would be interesting for further potential applications.

## **LIMITATION OF STUDY**

The spin coating technique is being improved to get single dispersed nanowire for electrical measurements followed by lithography. Therefore electrical properties of the p-n junction NW will have to be further evaluated.

## **ACKNOWLEDGEMENT**

We are grateful to the Ecole Polytechnique for financing the postdoctoral of Rashmi Rani.

## **AUTHOR CONTRIBUTIONS**

All authors have contributed equally.

## **DECLARATION OF INTERESTS**

The authors declare no competing interests.

## **FIGURES TITLE AND LENGENDS**

**Figure 1. X-ray diffraction patterns of Bi<sub>2</sub>Te<sub>3</sub>, Sb<sub>2</sub>Te<sub>3</sub> and p-n junction NWs imbedded in polycarbonate.**

(A) Combined XRD graph of Bi<sub>2</sub>Te<sub>3</sub>, Sb<sub>2</sub>Te<sub>3</sub> and p-n junction NWs imbedded in polycarbonate membrane note that the peaks at ~ 17° and ~ 38° correspond to the polymer and gold respectively. Two areas (blue) between 24-30° and 40-46° 2θ is taken for zoom graph for clear visibility of the peaks of each three samples (B, C) Zoom graph of Bi<sub>2</sub>Te<sub>3</sub>, Sb<sub>2</sub>Te<sub>3</sub> and p-n junction NWs in the range 24-32° 2θ showing peak orientation (B) in the range 40-46° 2θ(C). (D) Halder-Wagner plots used to micro-strain analysis in the Bi<sub>2</sub>Te<sub>3</sub>, Sb<sub>2</sub>Te<sub>3</sub> and p-n junction NWs.

**Figure 2. SEM and STEM -BF image of Bi<sub>2</sub>Te<sub>3</sub>NWs (a), Sb<sub>2</sub>Te<sub>3</sub>NWs (b) and p-n junction NWs.**

(A, B, C) SEM image of Bi<sub>2</sub>Te<sub>3</sub> NWs (A), Sb<sub>2</sub>Te<sub>3</sub> NWs (B) and p-n junction NWs (C) on silicon wafer after dissolving the polycarbonate membrane in CH<sub>2</sub>Cl<sub>2</sub> solution. (D, E, F) STEM-BF

images of Bi<sub>2</sub>Te<sub>3</sub> NWs (D), Sb<sub>2</sub>Te<sub>3</sub> NWs (E) and p-n junction NWs (F) on carbon grid after dissolving the polycarbonate membrane in CH<sub>2</sub>Cl<sub>2</sub> solution.

**Figure 3. GIXRD of p-n junction NWs.**

(A) Diagram showing the technique of GIXRD used for Bi-layer structure measurement in p-n junction NWs. (B) model displaying growth of p-n junction NWs inside the membrane. (C) Sketch of individual single p-n junction NW. (D) GIXRD of p-n junction NWs indicating layer structure correspond to Bi<sub>2</sub>Te<sub>3</sub> and Sb<sub>2</sub>Te<sub>3</sub>. Incidence angles ( $\omega$ ) taken from 3° to 6°.

**Figure 4. Elemental mapping of p-n junction NW.**

(A) Elemental mapping of the p-n junction single NW on carbon grid showing two components Sb<sub>2</sub>Te<sub>3</sub> and Bi<sub>2</sub>Te<sub>3</sub> respectively in single NW. (B) Bi (shown red), Sb (shown green) and Te (shown yellow) contents of the p-n junction NW. (C) Lateral hetero-junction (LHJ) identified in transition region in single p-n junction NW showing junction is abrupt (showed by black dotted line). (D) Enlarge image of the interface in p-n junction NW.

**Figure 5. Systematic diagram of dispersing p-n junction NWs by spin coating technique.**

(A) Top view SEM image of p-n junction NWs spreading on silicon wafer after dissolving AAO membrane in NaOH (B) Systematic diagram of spin-coating technique used for dispersing NWs for electronic application. (C, D) SEM image of p-n junction NWs after using spin coating at speed 1000 rpm (C) and at speed 2000 rpm (D).

**TABLE**

**Table 1.** Microstructural analysis for the Bi<sub>2</sub>Te<sub>3</sub>, Sb<sub>2</sub>Te<sub>3</sub> and p-n junction. D<sub>v</sub>(HW) and D<sub>v</sub>(S) for volume-weighted average crystallite sizes from Halder-Wagner and Scherrer formalisms respectively.



Sample	Dv (HW) (nm)	$\varepsilon$ (r.m.s.)	Dv (S) (nm)
Sb <sub>2</sub> Te <sub>3</sub>	24	0.0037	20
Bi <sub>2</sub> Te <sub>3</sub>	33	0	30
p-n junction	Bi <sub>2</sub> Te <sub>3</sub>	23	0
	Sb <sub>2</sub> Te <sub>3</sub>	30	0

## STAR METHOD TEXT

### RESOURCE AVAILABILITY

#### *Lead Contact*

Further information and requests for resources and materials should be directed to and will be fulfilled by the Lead Contact, Rashmi Rani (newton\_rashmi51@yahoo.com).

#### *Materials Availability*

This study did not generate new unique reagents.

#### *Data and Code Availability*

There is no dataset or code associated with this work.

## METHOD DETAILS

### Materials

Bismuth nitrate ( $\text{Bi}(\text{NO}_3)_3 \cdot 5\text{H}_2\text{O}$ , 99.997%, Sigma Aldrich chemicals, USA), Antimony chloride ( $\text{SbCl}_3$ , 99.997%, Sigma Aldrich chemicals, USA), Tellurium oxide ( $\text{TeO}_2$ , 99.997%, Sigma Aldrich chemicals, USA), Nitric acid ( $\text{HNO}_3$ , 70% , Sigma Aldrich chemicals, USA) and sodium hydroxide ( $\text{NaOH}$ , 98%, Sigma Aldrich chemicals, USA) were used as received. House distilled water was further purified through a Milli-Q (Millipore) filtration system. Acetone and ethanol were purchased from VWR. Si / $\text{SiO}_2$  were purchased from Sigma Aldrich. Anodic aluminium oxide membrane (AAO) of pore diameter  $\sim 80$  nm, pore length  $\sim 100$   $\mu\text{m}$  was purchased from In Redox materials innovation and Polycarbonate membrane of pore diameter  $\sim 47$  nm and pore length  $\sim 6$   $\mu\text{m}$  was purchased from Millipore Sigma.

### **Synthesis of $\text{Bi}_2\text{Te}_3$ , $\text{Sb}_2\text{Te}_3$ and p-n junction NWs**

In this work, we used two different types of membrane for template synthesis as required: Anodic aluminium oxide membrane (AAO) and Polycarbonate membrane. An AAO membrane was used for NWs formation in the following manner: first, through a mask, 100 nm of Au is sputtered on one side of the membrane using a sputtered coater (Quorum QT50TS) at 40 mA, to serve as a cathode (working electrode). The working electrode, is then connected with Ag paste, to Cu leads on a Plexiglas sample holder made in house. The contact electrode is then connected, with Au foil strips and Ag paste to another Cu leads on the same substrate. This assembly is wrapped in Kapton tape with the working electrode is exposed by an opening previously cut in the tape. The edges of the exposed contact electrode are sealed with nail polish. The exposed area of the membrane is a  $0.2 \text{ cm}^2$  circle. The same protocol was used for polycarbonate membrane [Wade and Wegrowe, 2005].

### **Electrodeposition of $\text{Bi}_2\text{Te}_3$ , $\text{Sb}_2\text{Te}_3$ and p-n junction NWs**

These NWs were fabricated by direct-current electrodeposition into AAO /polycarbonate membrane sample as prepared above. The plating solution was prepared by dissolving Te, Bi and Sb into 1 M HNO<sub>3</sub> was mixed for 24 hours at room temperature then the solution was diluted to desired volume with distilled water. The electrodeposition using AAO (50µm thick) was carried out at a constant potential of -62 mV for 1500 s for Bi<sub>2</sub>Te<sub>3</sub> NWs and -300 mV for 2000 s for Sb<sub>2</sub>Te<sub>3</sub> relative to an Ag/AgCl reference electrode at room temperature while for polycarbonate (6µm thick) the constant potential was for 500s and 650s for Bi<sub>2</sub>Te<sub>3</sub> and Sb<sub>2</sub>Te<sub>3</sub> respectively. A pure Au wire was used as a counter electrode and AAO/polycarbonate membrane was used as a working electrode. Crystalline NWs were obtained by dissolving the AAO and polycarbonate membrane with 2 M aqueous. NaOH solution and dichloromethane respectively. The as obtained product is centrifuged followed by washing with deionized water three-four times. The whole procedure is shown in [Figure S8]. For p-n junction nanowire we deposited n- type Bi<sub>2</sub>Te<sub>3</sub> with constant potential of -62 mV, time 500s in half of the wire and another half we deposited p-type Sb<sub>2</sub>Te<sub>3</sub> with constant potential of -300 mV, time 1000s. For polycarbonate membrane, the time was 50 s for Bi<sub>2</sub>Te<sub>3</sub> and 100 s for Sb<sub>2</sub>Te<sub>3</sub>.

### **Characterizations**


The structural properties of the NWs were analysed by X-ray diffraction (XRD), (XRD, D8 Advance, Bruker AXS) dedicated to thin film analysis, in a parallel beam geometry ( $\omega$ - $2\theta$ ) equipped with Cu radiation ( $K\alpha_1 = 1.54178 \text{ \AA}$ ). The data collection was performed from 21 to 50,  $2\theta$ , with a step of  $0.03^\circ$  and 15 seconds per step. Phase identification was performed with the highscore software (PANalytical) and powder diffraction files (ICDD PDF2 2004 and COD databases) [Grazulis et al., 2009]. Morphological properties of the wires were analysed with Scanning electron microscopy (SEM) Hitachi S-4800. The SEM imaging was performed at 10


kV and the sample were made by a solution of NWs was dispersed in 0.5 mL of absolute ethanol. A droplet was then drop cast onto a silicon substrate and naturally dried in air for 20 min. Selected Area Electron Diffraction (SAED) have been acquired on a JEOL 2010F operating at 200 kV. Scanning- TEM (STEM) experiments have been performed on a probe-corrected field emission gun FEI Titan Themis microscope operating at 200 kV (probe size 1Å). This microscope is equipped with the "Super-X" detector permitting quantitative elemental mapping of Sb, Bi and Te (Cliff-Lorimer methods) by EDX." The sample preparation for TEM was the same as for SEM except that the drop cast onto a Cu coated TEM grid (agar scientific.).

#### KEY RESOURCE TABLE

REAGENT or RESOURCE	SOURCE	IDENTIFIER
Chemicals, peptides, and recombinant proteins		
Bismuth nitrate	Sigma Aldrich chemicals, USA	CAS Number 10035-06-0
Antimony chloride	Sigma Aldrich chemicals, USA	CAS Number 10025-91-9
Tellurium oxide	Sigma Aldrich chemicals, USA	CAS Number 7446-07-3
Nitric acid	Sigma Aldrich chemicals, USA	CAS Number 7696-37-2
Sodium hydroxide	Sigma Aldrich chemicals, USA	CAS Number 1310-73-2
Acetone	VWR	CAS Number 67-64-1
Ethanol	VWR	CAS Number 64-17-5
Deposited data		
Bi <sub>2</sub> Te <sub>3</sub> - crystal structure	This paper	JCPDS card: 00-015-0863
Sb <sub>2</sub> Te <sub>3</sub> - crystal structure	This paper	JCPDS card: 00-015-0874
Membrane		
Anodic aluminum oxide	InRedox	CAS Number 1344-28-1
Polycarbonate membrane	Millipore Sigma	Catalog number DTTP04700

## REFERENCES

Alpichshev, Z., Analytis, J.G., Chu, J. H., Fisher, I.R., Chen, Y.L., Shen, Z.X., Fang, A., and Kapitulnik, A. (2010). STM Imaging of Electronic Waves on the Surface of Bi<sub>2</sub>Te<sub>3</sub>: Topologically Protected Surface States and Hexagonal Warping Effects. *Phys. Rev. Lett.* 104, 016401-5.  <https://doi.org/10.1103/PhysRevLett.104.016401>

Chen, Y.L., Analytis, J.G., Chu, J.H., Liu, Z.K., Mo, S.K., Qi, X.L., Zhang, H.J., Lu, D.H., Dai, X., Fang, Z., Zhang, S.C., Fisher, I.R., Hussain, Z., and Shen, Z.-X. (2009). Experimental Realization of a Three-Dimensional Topological Insulator, Bi<sub>2</sub>Te<sub>3</sub>. *Science*, 325, 178-181.  <https://doi.org/10.1126/science.1173034>

Eschbach, M., Mlynczak, E., Kellner, J., Kampmeier, J., Lanius, M., Neumann, E., Weyrich, C., Gehlmann, M., Gospodari, P., Dring, S., Mussler, G., Demarina, N., Luysberg, M., Bihlmayer, G., Schpers, T., Plucinski, L., Blgel, S., Morgenstern, M., Schneider, C.M., and Grtzmacher, D. (2015). Realization of a vertical topological p–n junction in epitaxial Sb<sub>2</sub>Te<sub>3</sub>/Bi<sub>2</sub>Te<sub>3</sub> heterostructures. *Nat. Commun.* 6, 8816-7. <https://doi.org/10.1038/ncomms9816>

Fang, H., Feng, T., Yang, H., Ruan, X., and Wu, Y. (2013). Synthesis and Thermoelectric Properties of Compositional-Modulated Lead Telluride–Bismuth Telluride Nanowire Heterostructure. *Nano Lett.* 13, 2058-2063. <https://doi.org/10.1021/nl400319u>


Fein, F., Wei, Z., Wang, Q., Lu, P., Wang, S., Qin, Y., Pan, D., Zhao, B., Wang, X., Sun, J., Wang, X., Wang, P., Wan, J., Zhou, J., Song, M.H.F., Wang, B., and Wang, G. (2015). Solvothermal synthesis of Lateral Heterojunction  $\text{Sb}_2\text{Te}_3/\text{Bi}_2\text{Te}_3$  Nanoplates. *Nano Lett.* 15, 5905-5911.

<https://doi.org/10.1021/acs.nanolett.5b01987>

Grazulis, S., Chateigner, D., Downs, R. T., Yokochi, A. F. T., Quirats, M., Lutterotti, L., Manakova, E., Butkus, J., Moeck, P., and Bail, A. Le. (2009). Crystallography Open Database – an-open-access collection of crystal structures. *J.Appl.Cryst.* 42, 726- 729.

<https://doi.org/10.1107/S0021889809016690>



Guo, Y., Li, Z., and Peng, H. (2015). A Roadmap for Controlled Production of Topological Insulator Nanostructures and Thin Films. *Small.* 11, 3290-3305. 

<https://doi.org/10.1002/sml.201403426>

Halder, N.C., and Wagner, C.N.J. (1966). Separation of particle size and lattice strain in integral breadth measurements. *Acta Cryst.* 20, 312-313.

<https://doi.org/10.1107/S0365110X66000628>

Hasan, M.Z., and Kane, C.L. (2010). Colloquium: Topological insulators. *Rev. Mod. Phys.* 82, 3045-3067. <https://doi.org/10.1103/RevModPhys.82.3045>

Hasan, M.Z., and Moore, J.E. (2011). Three-Dimensional Topological Insulators. *Annu. Rev. Condens. Matter Phys.* 2, 55-78. <https://doi.org/10.1146/annurev-conmatphys-062910-140432>.

Hong, S.S., Zhang, Y., Cha, J.J., Qi, X.L., and Cui, Y. (2014). One-Dimensional Helical Transport in Topological Insulator Nanowire Interferometers. *Nano Lett.* 14, 2815-2821. <https://doi.org/10.1021/nl500822g>

Hsieh, D., Xia, Y., Qian, D., Wray, L., Meier, F., Dil, J.H., Osterwalder, J., Patthey, L., Fedorov, A.V., Lin, H., Bansil, A., Grauer, D., Hor, Y.S., Cava, R.J., and Hasan, M.Z. (2009). Observation of Time-Reversal-Protected Single-Dirac-Cone Topological-Insulator States in  $\text{Bi}_2\text{Te}_3$  and  $\text{Sb}_2\text{Te}_3$ . *Phys. Rev. Lett.* 103, 146401-4. <https://doi.org/10.1103/PhysRevLett.103.146401>

Ida, T., Shimazaka, S., Hibino, H., and Toraya, H. (2003). Diffraction peak profiles from spherical crystallites with lognormal size distribution. *J. Appl. Cryst.* 36, 1107-1115. <https://doi.org/10.1103/PhysRevLett.115.096802>

Ilan, R., Juan, F. D., and Moore, J.E. (2015). Spin-Based Mach-Zehnder Interferometry in Topological Insulator p-n Junctions. *Phys. Rev. Lett.* 115, 096802-5. <https://doi.org/10.1103/PhysRevLett.115.096802>


Izumi, F., and Ikeda, T. (2004). Advance ceramic research centre Annual report. 3, 33-38.

Jiang, X., Zhang, X., Wang, Y., Wang, N., West, D., Zhang, S., and Zhang, Z. (2015). Tunable GaTe- MoS<sub>2</sub> van der Waals p-n Junctions with Novel Optoelectronic Performance. Nano Lett. 15, 3147-3152. <https://doi.org/10.1021/acs.nanolett.5b03291>


Kim, M-Y., and Oh, T-S. (2010) Crystallization behavior and thermoelectric characteristics of the electrodeposited Sb<sub>2</sub>Te<sub>3</sub> thin films. Thin Solid Films. 518, 6550-6553. <https://doi.org/10.1016/j.tsf.2010.03.052>

Kong, D., Randel, J.C., Peng, H., Cha, J.J., Meister, S., Lai, K., and Chen, Y. (2010). Topological Insulator Nanowires and Nanoribbons. Nano Lett. 10, 329-333. <https://doi.org/10.1021/nl903663a>

Krieg, J., Giraud, R., Funke, H., Dufouleur, J., Escoffier, W., Trautmann, C., and Toimil-Molares, M.E. (2019). Magnetotransport measurements on Bi<sub>2</sub>Te<sub>3</sub> nanowires electrodeposited in etched ion-track membranes. J. Phys. Chem. Solids. 128, 360-366. <https://doi.org/10.1016/j.jpcs.2018.02.002>

Langford, J.I., and Wilson, A.J.C. (1978). Scherrer after sixty years: A survey and some new results in the determination of crystallite size. J. Appl. Cryst. 11, 102-113.  <https://doi.org/10.1107/S0021889878012844>

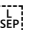


Le, P.H., Tzeng, W. Y. Chen, H. J. Luo, C.W., Lin, J.Y., and Leu, J. (2014). Superconductivity in textured Bi clusters/  $\text{Bi}_2\text{Te}_3$  films. *APL Mater.* 2, 096105-096107.   
<https://doi.org/10.1063/1.4894779>

Le, P.H., Liu, P.T., Luo, C.W., Lin, J.Y. & Wu, K.H. (2017). Thickness-dependent magnetotransport properties and terahertz response of topological insulator  $\text{Bi}_2\text{Te}_3$  thin films. *J. Alloys and Comps.* 692,972-979. <https://doi.org/10.1063/1.4894779>

Lensch-Falk, J.L., Banga, D., Hopkins, P.E., Robinson, D.B., Stavila, V., Sharma, P.A., and Medlin, D.L. (2012). Electrodeposition and characterization of nano-crystalline antimony telluride thinfilms. *Thin Solid Films.* 520, 6109-6117. <https://doi.org/10.1016/j.tsf.2012.05.078>

Liu, P., Willian, J.R., Cha, J.J (2019). Topological Nanomaterials. *Nat Rev Mater.* 4, 479–496. <https://doi.org/10.1038/s41578-019-0113-4>

Luo, C.W., Wang, H.J., Ku, S.A., Chen, H.J., Yeh, T.T., Lin, J.Y., Wu, K.H., Juang, J.Y., Young, B.L., Kobayashi, T., Cheng, C.M., Chen, C.H., Tsuei, K.D., Sankar, R., Chou, F.C., Kokh, K.A., Tereshchenko, O.E., Chulkov, E.V., Andreev, Y.M., and Gu, G.D. (2013). Snapshots of Dirac Fermions near the Dirac Point in Topological Insulators. *Nano Lett.* 13, 5797-5802. <https://doi.org/10.1021/nl402184z>

Ma, C., Ding, Y., Moore, D., Wang, X. D., and Wang, Z.L. (2004). Single-Crystal CdSe Nanosaws. *J. Am. Chem. Soc.* 126, 708- 709. <https://doi.org/10.1021/ja0395644>

Moore, J.E., and Balents, L. (2007). Topological invariants of time-reversal-invariant band structures. *Phys. Rev. B.* 75, 121306-4. <https://doi.org/10.1103/PhysRevB.75.121306>

Moore, J.E. (2010). The birth of topological insulators. *Nature.* 464, 194-8. <https://doi.org/10.1038/nature08916>

Park, Y.S., and Lee, J.S. (2014). Synthesis of single-crystalline topological insulator  $\text{Bi}_2\text{Se}_3$  nanomaterials with various morphologies *J. Nanoparticle Research.* 16, 2226-7.

<https://doi.org/10.1007/s11051-013-2226-9>

Pinisetty, D., Gupta, M., Karki, A. B., Young, D. P., and Devireddy, R.V. J. (2011). Fabrication and characterization of electrodeposited antimony telluride crystalline nanowires and nanotubes. *J. Mater. Chem.* 21, 4098-4107. <https://doi.org/10.1039/C0JM01969K>

Qi, X.L., and Zhang, S.C. (2011). Topological insulators and superconductors. *Rev. Mod. Phys.* 83, 1057-1110. <https://doi.org/10.1103/RevModPhys.83.1057>

Tu, C. M., Yeh, T. T., Tzeng, W.Y., Chen, Y. R., Chen, H. J., Ku, S.A., Luo, C.W., Lin, J.Y., Wu, K. H., Juang, J. Y., Kobayashi, T., Cheng, C.M., Tsuei, K.D., Berger, H., Sankar, R., and Chou, F. C. (2015). Manifestation of a Second Dirac Surface State and Bulk Bands in THz Radiation from Topological Insulators. *Sci. Rep.* 5, 14128-14136. <https://doi.org/10.1038/srep14128>

Wade, T. L., and Wegrowe, J. -E. (2005). Template synthesis of nanomaterials. *Eur. Phys. J. Appl. Phys.* 29, 3-22. <https://doi.org/10.1051/epjap:2005001>

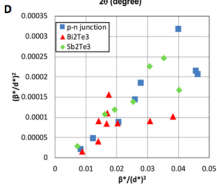
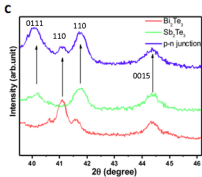
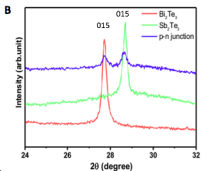
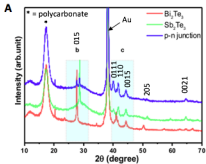
Wang, G., Zhu, X.G., Sun, Y.Y., Li, Y.Y., Zhang, T., Wen, J., Chen, X., He, K., Wang, L.L., Ma, X.C., Jia, J.F., Zhang, S.B., and Xue, Q.K. (2011). Topological Insulator Thin Films of  $\text{Bi}_2\text{Te}_3$  with Controlled Electronic Structure. *Adv. Mater.* 23, 2929-2932. <https://doi.org/10.1002/adma.201100678>

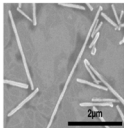
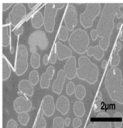
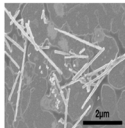
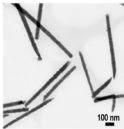
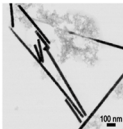
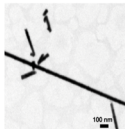
Xie, S., Ouyang, Z., Jia, B., and Gu, M. (2013). Large-size, high-uniformity, random silver nanowire networks as transparent electrodes for crystalline silicon wafer solar cells. *Optics Express.* 21, 355-362. <https://doi.org/10.1364/OE.21.00A355>

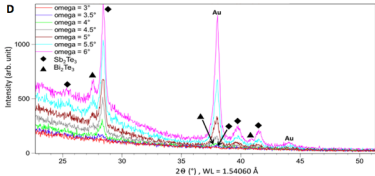
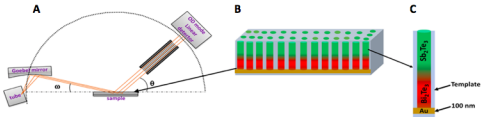
Zhang, T., Cheng, P., Chen, X., Jia, J. F., Ma, X., He, K., Wang, L., Zhang, H., Dai, X., Fang, Z., Xie, X., and Xue, Q. K. (2009). Experimental Demonstration of Topological Surface States Protected by Time-Reversal Symmetry *Phys. Rev. Lett.* 103, 266803-4. <https://doi.org/10.1103/PhysRevLett.103.266803>

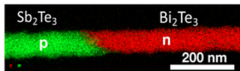
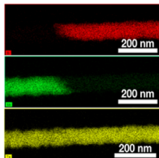
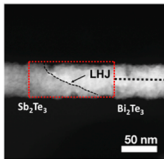
Zhang, Y., Snedaker, M.L., Birkel, C.S., Mubeen, S., Ji, X., Shi, Y., Liu, D., Liu, X., Moskovits, M., and Stucky, G.D. (2012). Silver-based intermetallic heterostructures in  $\text{Sb}_2\text{Te}_3$  thick films with enhanced thermoelectric power factors. *Nano Lett.* 12, 1075-1080. <https://doi.org/10.1021/nl204346g>

Zuev, Y.M., Lee, J.S., Galloy, C., Park, H., and Kim, P. (2010). Diameter Dependence of the Transport Properties of Antimony Telluride Nanowires. *Nano Lett.* 10, 3037-3040. <https://doi.org/10.1021/nl101505q>



**A****B****C****D****E****F**



**A****B****C****D**